Solid-solid phase transitions across orientationally disordered phases: The case of tetrachloro-*m*-xylene

Jonathan F. Gebbia,[1,2,*] Ares Sanuy,[1,2] Michela Romanini,[1,2] David Aguilà,[3] Phillipe Negrier,[4] Stephane Massip,[5] María del Barrio,[1,2] Felix Fernandez-Alonso,[6,7,8] Sanghamitra Mukhopadhyay,[9] Markus Appel,[10] Claudio Cazorla,[1,2,11] Luis Carlos Pardo,[1,2] and Josep Lluís Tamarit[1,2]

[1]*Grup de Caracterització de Materials, Departament de Física, EEBE, Universitat Politècnica de Catalunya, Eduard Maristany, 10-14, 08019 Barcelona, Catalonia, Spain*

[2]*Barcelona Research Center in Multiscale Science and Engineering, Universitat Politècnica de Catalunya, Eduard Maristany, 10-14, 08019 Barcelona, Catalonia, Spain*

[3]*Departament de Química Inorgànica, and Institute of Nanoscience and Nanotechnology (IN2UB), Universitat de Barcelona, Barcelona, Spain*

[4]*Laboratoire Ondes et Matière d'Aquitaine, Université de Bordeaux, UMR 5798, F-33400 Talence, France*

[5]*Institut Européen Chimie & Biologie, Universite de Bordeaux, CNRS UMS 3033, INSERM US001, F-33607 Pessac, France*

[6]*Centro de Física de Materiales (CFM-MPC), CSIC-UPV/EHU, Paseo de Manuel Lardizabal 5, 20018 Donostia, Gipuzkoa, Spain*

[7]*Donostia International Physics Center (DIPC), Paseo de Manuel Lardizabal 4, 20018 Donostia, San Sebastian, Spain*

[8]*IKERBASQUE, Basque Foundation for Science, Plaza Euskadi 5, 48009 Bilbao, Spain*

[9]*ISIS Neutron and Muon Source, Rutherford Appleton Laboratory, Chilton, Didcot, Oxfordshire OX11 0QX, United Kingdom*

[10]*Institut Laue-Langevin (ILL), 71 Av. Des Martyrs, 38000 Grenoble, France*

[11]*Institució Catalana de Recerca i Estudis Avançats (ICREA), Passeig Lluís Companys 23, 08010 Barcelona, Spain*

(Received 17 October 2025; accepted 2 January 2026; published 2 February 2026)

We uncover a previously unreported solid-solid phase transition in tetrachloro-*m*-xylene (TCMX), a hexa-substituted benzene derivative exhibiting orientational disorder. Differential scanning calorimetry and powder x-ray diffraction reveal a weak but reproducible phase transition near 437 K, corresponding to a continuous, second-order symmetry change from monoclinic $P2_1/n$ (phase II) to orthorhombic *Pnnm* (phase I). Despite this structural reorganization, quasielastic neutron scattering demonstrates that molecular dynamics remain governed by discrete 60° in-plane reorientational jumps consistent with the pseudosixfold molecular symmetry. The activation energy is unaffected, while only slight variations in relaxation times and effective rotational radii are detected. Molecular dynamics simulations reproduce the transition and clarify its microscopic origin. In phase II, weak orientational correlations between adjacent molecular columns are present, but these constraints vanish in phase I, restoring higher symmetry without altering the underlying reorientational mechanism. This study establishes TCMX as a rare example of a disorder-disorder transition in which molecular dynamics are preserved while collective orientational correlations reorganize. More broadly, our results highlight how subtle symmetry changes govern emergent behavior in disordered crystals, advancing the understanding of plastic phases and phase transitions in complex condensed matter systems.

DOI: 10.1103/pcsf-sfml

I. INTRODUCTION

Orientationally disordered molecular crystals, commonly known as plastic crystals, occupy an intermediate regime between liquids and fully ordered crystals. These systems retain long-range translational order while exhibiting rotational disorder at the molecular level [1]. Compared to the liquid phase, where both translational and rotational degrees of freedom are fully activated [2], plastic crystals exhibit a reduced configurational complexity. This relative simplification makes them ideal systems to study collective rotational processes, which are often more difficult to isolate and interpret in fully disordered liquids. Moreover, such systems are key to understanding the interplay between structural long-range translational order and molecular mobility and are known to exhibit a wide range of solid-solid transitions, including order-disorder and disorder-disorder transformations [3–9].

Plastic crystals are typically associated with systems in which molecular reorientation is nearly isotropic, allowing for continuous rotational freedom. However, a significant subset of these materials exhibit restricted reorientational dynamics, where the motion is limited to discrete jumps between energetically equivalent orientations. This behavior arises from the compatibility between the molecular symmetry and the site symmetry of the underlying crystal lattice, which defines a set of symmetry-related equilibrium orientations. As a result, certain atomic positions acquire fractional occupancy factors in the crystallographic structure, giving rise to a form of statistical orientational disorder. These systems preserve

*Contact author: jonathan.fernando.gebbia@upc.edu

the hallmark features of plastic crystals while offering a well-defined framework to investigate symmetry-governed reorientational dynamics.

Representative examples include the family of halomethane crystals CBr_nCl_{4-n} $(n = 0, 1, 2)$ [10–15], low-temperature phases of some adamantane derivatives such as 2-O-adamantanone [16–20] and 1-F-adamantane [21–23], and hexasubstituted benzene derivatives such as pentachloronitrobenzene [24–27], all of which exhibit discrete reorientational dynamics governed by molecular symmetry. These systems have previously been studied in detail, allowing us to establish a robust framework for understanding orientational disorder and symmetry-constrained dynamics in molecular crystals.

Another representative example, and the subject of the present study, is tetrachloro-*m*-xylene [$C_6Cl_4(CH_3)_2$, IUPAC name 1,2,3,5–tetrachloro–4,6–dimethylbenzene (TCMX)], a molecular crystal that also belongs to the family of hexasubstituted benzenes [28]. The TCMX molecule consists of a benzene ring substituted with four chlorine atoms and two methyl groups in meta positions. At room temperature, TCMX exhibits a low-temperature solid monoclinic phase II with space group $P2_1/n$ and $Z = 2$ molecules/unit cell. The disorder related to this solid phase was attributed to a six quasiequivalent in-plane molecular orientations related to rotational jumps of 60° around a six-fold-like axis perpendicular to the molecular plane. The disorder, then, is statistical and confers to chlorine atoms and methyl groups fractional occupational factors of $f_{Cl} = 4/6$ and $f_{CH_3} = 2/6$. The melting point of TCMX was reported at 496 K with no intermediate solid-solid transition reported prior the melting.

In this work, we reveal a previously undetected phase transition between two orientationally disordered crystalline phases of TCMX. Differential scanning calorimetry (DSC) and x-ray diffraction measurements identify a subtle but well-defined transformation at $T_{II\text{-}I} = 437 \pm 1$ K from the low-temperature phase II to a high-temperature phase I, consistent with a continuous, second-order group-subgroup transition. The thermodynamic signature of this transition is weak, highlighting the need for a dynamic probe to fully understand its nature.

To characterize the dynamics across the transition, we performed quasielastic neutron scattering (QENS) measurements. These experiments show that molecular reorientations are already active below the transition (phase II) and remain the dominant process throughout, consisting of discrete 60° jumps among symmetry-equivalent orientations. The activation energy remains essentially constant across the phase transition, while the characteristic timescales vary slightly with temperature and symmetry. This confirms that the II → I phase transition does not involve a change in the underlying mechanism, but rather a subtle reorganization of the reorientational landscape which gives rise to a change of the spatial group for phase I. We use MD to explore the orientation and position of molecules at different temperatures, going beyond crystallographic averages. Specifically, we analyze the orientation of each molecule with respect to the crystallographic axes, and the relative orientation and position between molecular pairs, to assess whether the transition involves collective reorganization. This detailed analysis allows us to identify the emergence (or loss) of orientational correlations between molecules, and to clarify the microscopic origin of the symmetry change observed experimentally.

II. METHODS

TCMX (tetrachloro-*m*-xylene) was purchased from two different suppliers: Dr. Ehrenstorfer GmbH (with purity greater than 99.5%) and Chem-Space Delivering Discovery (with purity greater than 99%). Both batches exhibited an indistinguishable physical appearance, consisting of white, very small needle-shaped crystallites. The samples were used as received without any additional purification.

During the study of the TCMX compound, different experimental techniques were used: powder and single-crystal x-ray diffraction (XRD), DSC, and QENS.

A. Single-crystal x-ray diffraction

Data for TCMX at 100 K (phase II) were collected on a Bruker APEX II QUAZAR diffractometer equipped with a microfocus multilayer monochromator with Mo Kα radiation ($\lambda = 0.71073$ Å). The crystal was mounted with Paratone N grease on a MiTeGen kapton loop and placed in the N_2 stream of an Oxford Cryosystems Cryostream. Data reduction and absorption corrections were performed with SAINT and SADABS, respectively [29]. The structure was solved by intrinsic phasing with SHELXT [30], and refined by full-matrix least-squares on F^2 with SHELXL [31], through Olex2 [32]. All nonhydrogen atoms were refined anisotropically. Cl and C (from methyl groups) were refined disordered with 0.66666/0.33333 occupancies, respectively. Hydrogen atoms were placed geometrically using AFIX 137, which provided more realistic anisotropic displacement parameters for the corresponding carbon atoms, and confirmed by Fourier synthesis. However, all H atoms were included in the structure factor calculations. Details can be found in CCDC 2490401, which contains the corresponding supplementary crystallographic data [33,34].

B. Powder x-ray diffraction

High-resolution powder x-ray diffraction (PXRD) patterns on TCMX were collected with a vertically mounted INEL cylindrical position-sensitive detector (CPS–120) using the Debye-Scherrer geometry and transmission mode providing an angular step of 0.029° (2θ) between 4° and 120°. Monochromatic Cu-Kα_1 radiation ($\lambda = 1.5406$ Å) was employed, selected by means of a focusing incident-beam germanium monochromator. Prior to loading, the powder was gently ground to reduce crystallite size and minimize potential morphology-related effects. Powder sample were loaded into 0.5 mm diameter Lindemann capillaries, which were rotated during measurements to suppress possible preferred-orientation effects and ensure proper averaging over crystallite orientations. Temperature-dependent PXRD patterns were acquired from 100 to 470 K, in steps of 10–20 K, using an Oxford Cryosystems Cryostream Cooler (700 series) based on liquid nitrogen flow. External calibration was performed with a mixture of $Na_2Ca_2Al_2F_{14}$ and silver behenate, with cubic spline fitting applied to convert detector channels into

2θ values. Lattice parameters of the low-temperature phase II were extracted at each temperature via Pawley matching procedures. As for the high-temperature phase I, the indexing of the PXRD patterns, structure solution, Pawley and Rietveld refinements were performed using Materials Studio Program. Rietveld refinement was performed using an initial rigid-body constraint, involving all atoms with a single overall isotropic displacement parameter. CIF file of TCMX at 460 K was deposited at Cambridge Crystallographic Data Centre as 2485464 [34].

C. Differential scanning calorimetry

Calorimetric measurements were performed using a DSC Q100 instrument from TA Instruments in standard heat-flow mode. Approximately 5.56 mg of TCMX were sealed in a hermetic aluminum pan with a matching lid to prevent sublimation and ensure the integrity of the sample during the thermal cycle. The temperature range ranged from 400 to 510 K at a constant rate of 10 K min^{-1}. Both heating and cooling scans were recorded to assess the reversibility of thermal events. The instrument was calibrated for temperature and enthalpy using indium as a standard prior to the experiments.

D. Quasielastic neutron scattering

QENS experiments were performed using two complementary instruments to access different dynamical windows: the OSIRIS time-of-flight spectrometer [35–38] at the ISIS Neutron and Muon Source (UK) and the IN16B backscattering spectrometer at the Institut Laue-Langevin (ILL, France).

1. OSIRIS—time-of-flight spectrometer

The OSIRIS spectrometer was operated in high resolution mode using a 002 plane of a pyrolithic graphite monochromator (PG002), providing an energy resolution of approximately $\delta E \approx 25.4$ μeV (full width at half maximum) and a dynamic range of $\Delta E = \pm 0.4$ meV, with a momentum transfer range of $0.18 \leqslant Q \leqslant 1.8$ Å^{-1}. Approximately 2 g of TCMX (Dr. Ehrenstorfer GmbH, purity > 99.5%) in powdered form was packed into a sealed aluminum sachet and mounted in an annular aluminum can with a total thickness of 1 mm, corresponding to about 15% neutron transmission.

An initial elastic window scan (EWS) was used to identify the temperature range in which molecular dynamics enters the instrumental time window. After identifying the relevant temperature range, a series of quasielastic spectra were collected between 408 and 453 K in steps of 5 K, covering the region across the II → I phase transition. Each temperature point was measured for a sufficient acquisition time to ensure reliable statistics.

Data reduction was carried out using the Mantid software [39]. Spectral analysis involved convolution of the theoretical model with the instrumental resolution. The number of Lorentzian components required to reproduce the observed quasielastic signal, $S_{\text{obs}}(Q, \omega)$, was determined using the FABADA algorithm, a homemade Bayesian fitting code [40,41]. This method enables a statistically robust identification of the minimal model consistent with the experimental data.

2. IN16B—High-resolution backscattering spectrometer

Complementary QENS measurements were performed on the IN16B backscattering spectrometer to extend the accessible time window toward slower dynamics. IN16B operates in high-resolution mode with an energy resolution of $\delta E \approx 0.75$ μeV (full width at half maximum) and a dynamic range of $\Delta E \approx \pm 30$ μeV, covering a momentum transfer range of $0.2 \leqslant Q \leqslant 1.9$ Å^{-1} (standard setup with Si111 monochromator and analysers). This significantly improved resolution compared to OSIRIS allows probing molecular dynamics on the nanosecond timescale, yet at the expenses of a more restricted dynamic range.

Approximately 1.0−1.5 g of TCMX (Chem-Space, purity > 99%) was loaded following the same protocol as for OSIRIS, i.e., the powdered material was sealed in an aluminum sachet and mounted in an annular aluminum can.

Data acquisition followed a two-step procedure. First, temperature-dependent *elastic fixed window scans* (EFWS) and *inelastic fixed window scans* (IFWS) were performed to identify the onset of molecular dynamics within the instrumental time window [42]. EFWS involved monitoring the elastic intensity at $E = 0$ as a function of temperature, whereas IFWS measured the inelastic intensity at two fixed energy offsets ($E = 3$ μeV and $E = 6$ μeV), providing complementary insight into the activation of reorientational processes. After these preliminary scans, high-resolution quasielastic spectra were collected at selected temperatures across the II → I phase transition.

All data reduction and analysis, including EFWS/IFWS trends and full QENS spectra fitting, were carried out using the Mantid software package [39,43]. The observed QENS spectra, $S_{\text{obs}}(Q, \omega)$, were modeled by convolution of the theoretical scattering function with the experimental resolution, using the same approach as for OSIRIS.

E. Molecular dynamics

Classical molecular dynamics (MD) simulations were conducted using the GROMACS package with a CHARMM force field [44–46]. Both bonded and nonbonded interactions are explicitly defined within this force field and described in detail in the cited references. The temperature and pressure were controlled using the velocity-rescale thermostat (v-rescale, $\tau_t = 0.5$ ps) and the canonical-rescale (C-rescale) barostat ($\tau_p = 1$ ps), respectively. In this parametrization, the motion of the hydrogens in the methyl groups is governed by the corresponding dihedral potential. However, at the temperatures simulated in this study, this barrier is sufficiently small for the methyl groups to rotate almost freely, showing only a slight preference for orientations consistent with the underlying C_{3v} symmetry. Short-range electrostatic and van der Waals interactions were computed using a cutoff of 0.7 nm, whereas long-range electrostatics were treated with the particle-mesh Ewald method, using default GROMACS parameters and achieving a real-space force accuracy of approximately 10^{-4} kcal mol^{-1} Å^{-1}.

To build a realistic atomistic model suitable for molecular-dynamics simulations, we first reconstructed the crystalline structure obtained from the Rietveld refinement from the diffraction data which contains the full crystallographic

information to generate the molecular positions and orientations within a single unit cell. From this experimentally derived unit cell, we constructed a $4 \times 2 \times 2$ simulation supercell containing a total of 288 TCMX molecules. This supercell was used as the initial state for the MD protocol, which consisted of three stages. First, the system was thermalized in the NVT ensemble for 20 ps (10 000 steps with a 2 fs time step) to remove any high-energy contacts. The simulation was then switched to NPT conditions and equilibrated for 100 ns using a 1 fs step (10^8 integration steps), allowing both the density and the cell dimensions to fully relax. Finally, a 5 ns production run was performed in the NPT ensemble with a 10 fs time step. Trajectory frames were saved every 0.05 ps, and energies every 10 ps. From the production segment, 1,000 configurations were selected at equal time intervals, sufficiently separated to be statistically independent, and used for structural and orientational analyses.

To map the full thermal response, additional production runs were carried out at temperatures from 200 K to 400 K in 5 K increments. Once all simulation trajectories were generated, we used the ANGULA freely available software [47] to analyze and quantify the relevant observables, including angular distributions and radial distribution functions $g(r)$. These outputs served as the basis for the maps, histograms, and structural descriptors presented next in Sec. III, which are independent of the selected lattice-fixed reference system. Due to the structural complexity of TCMX and the inherent technical limitations of MD simulations (i.e., relatively reduced supercells and short simulation times), we have not attempted to theoretically identify the lattice vectors and symmetry properties of the disordered phases.

III. RESULTS

A. DSC

Figure 1 shows the DSC thermogram of TCMX recorded upon heating and cooling between 400 and 510 K. At first sight, the thermogram appears to exhibit a single prominent endothermic peak corresponding to the melting transition near 496 K (onset temperature), consistent with previous reports [28]. No other major thermal effects are observed in the main plot.

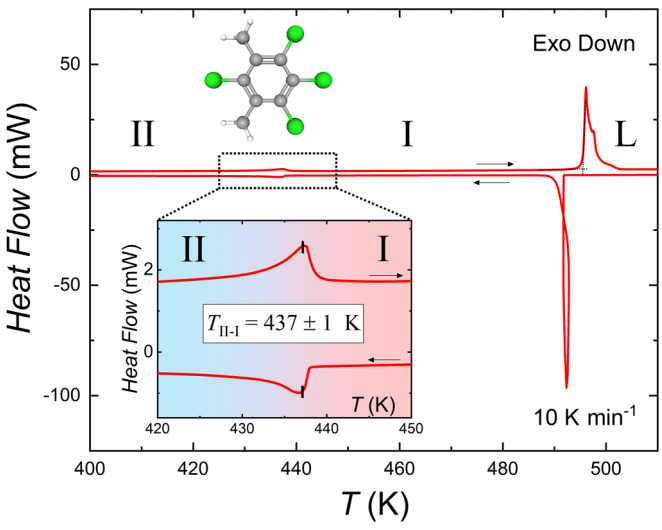

FIG. 1. DSC thermogram of TCMX from 400 to 510 K during a heating and cooling ramp with a rate of 10 K min^{-1}. Sequence of phases II–I–L is indicated. Inset: zoom of the II–I phase transition signal with the measured peak temperature.

However, a closer inspection of the region between 420 and 450 K (inset of Fig. 1) reveals a subtle but well-defined thermal feature that had previously gone unnoticed in the literature. This anomaly occurs at $T_{\text{II-I}} = 437 \pm 1$ K (peak temperature on heating) and is fully reversible upon cooling, with the transition onset occurring at virtually the same temperature, ruling out a kinetic origin, such as the freezing of residual orientational disorder. Instead, this signature points to a genuine thermodynamic phase transition between two crystalline states hereafter referred to as low-temperature phase II and high-temperature phase I (see PXRD analysis).

The thermal effect is extremely weak and extended in temperature, in line with the features displayed for a second-order transition, where the heat flow anomaly primarily reflects a discontinuity in heat capacity rather than a latent heat effect. Furthermore, the absence of measurable thermal hysteresis (thermal effects on heating and on cooling peak at the same temperature) supports the interpretation of a continuous and reversible transformation. The enthalpy change (calculated as $\int C_p\, dT$) associated with the excess heat capacity of the II $\rightarrow$ I phase transition is about 8 J g^{-1}, which corresponds to an entropy change of approximately $0.5R$. Although this value is close to $R \ln 2$, which would correspond to doubling the number of configurations in phase I with respect to phase II, the change in the number of configurations between the two phases is elusive, due to the disordered character of low-temperature phase II. Based on these observations, we identify a phase sequence of phase II $\rightarrow$ phase I $\rightarrow$ Liquid, where only phase II was previously reported as an orientationally disordered state.

This subtle thermal feature motivates further structural and dynamical studies presented in the following sections, which aim to determine the underlying microscopic nature of this phase transition.

B. X-ray diffraction

The lattice paramenters and the space group of TCMX was previously determined by Khotsyanova *et al.* [48]. As described by Brock and Fu [28], most of the $C_6Cl_n(CH_3)_{6-n}$ derivatives are isostructural (standard space group No. 14, $P2_1/c$,), although they have been described in the literature by different settings of the space group. For clarity, in this article we adopt the setting $P2_1/n$ and all structural data and refinements are therefore reported in this setting. Single crystals of TCMX were picked up from the received powder. The corresponding single-crystal data collection and refinement parameters at 100 K are summarized in Table S1 of the Supplemental Material [33]. Virtually identical results were obtained from the Rietveld refinement of the powder x-ray diffraction (see details on Table S2 at the Supplemental Material [33]).

Figure 2 shows the projections of the single-crystal structure at 100 K (in the $P2_1/n$ setting) along the a^* [Fig. 2(a)] and b [Fig. 2(b)] directions. The molecules in the $P2_1/n$ group

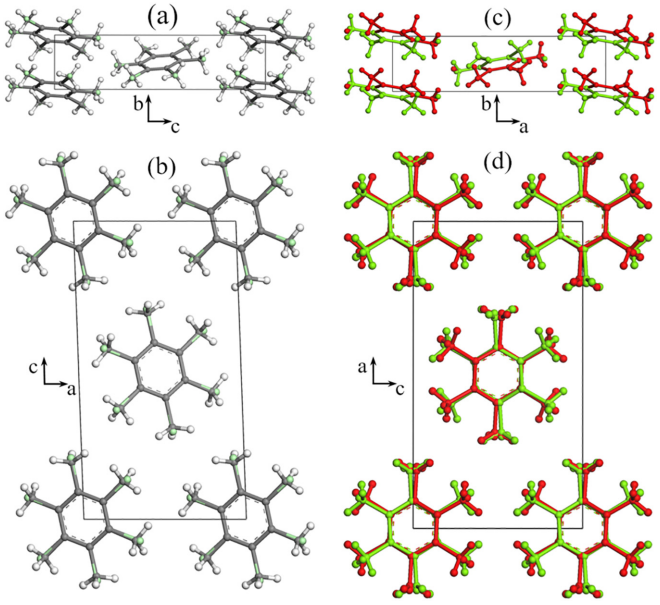

FIG. 2. X-ray crystal structures of TCMX in phase II at 100 K [panels (a) and (b), $P2_1/n$ setting] and in phase I at 460 K [panels (c) and (d)]. Panels (a) and (c) show projections along a^* and c^* axes, respectively, while panels (b) and (d) show projections along the b axes.

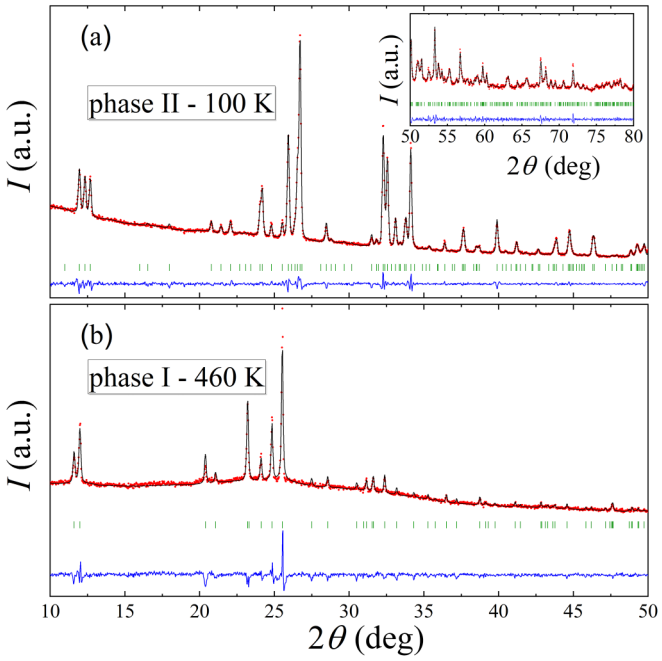

FIG. 3. Experimental (red circles) and calculated (black line) powder x-ray diffraction patterns along with the difference profile (blue line) and Bragg reflections (vertical sticks) of monoclinic $P2_1/n$ space group at 100 K (a) and of the orthorhombic $Pnnm$ space group at 460 K (b). Inset in (a) shows the data in 2θ range between 50° and 80° with intensities magnified by a factor of four.

occupy two symmetry-related inversion centers within the unit cell: one centered at (0,0,0) and the other at $(a/2, b/2, c/2)$. In this way, molecular stacking can be viewed as two columns running along the b axes, one formed by molecules at (0,0,0) and the other by those at $(a/2, b/2, c/2)$ [see Figs. 2(a) and 2(b)]. In addition, the molecules exhibit in-plane orientational disorder, with site occupancies of 4/6 for the Cl atoms and 2/6 for the CH_3 groups. This type of disorder leads to a reorientation of the molecular dipole, which has enabled characterization via dielectric spectroscopy [49], and even the observation of low-temperature glassy behavior [27], as this phase II persists down to temperatures below 1 K.

A representative long-time acquisition powder x-ray diffraction pattern at 100 K of phase II is shown in Fig. 3(a), together with the corresponding Rietveld refinement. Lattice parameters as a function of temperature for phase II are collected in Table S3 (see Supplemental Material [33]), together with the unit cell volume. When increasing temperature and approaching the thermal effect (Fig. 1), the β parameter decreases until it reaches the value of 90°, and thus new symmetries emerge. The structure of the new phase I was solved by means of Rietveld refinement of the powder x-ray diffraction data acquired at 460 K [Fig. 3(b)]. Results of this refinement can be found in Table S2 (see Supplemental Material [33]). The structure of phase I is orthorhombic, space group $Pnnm$. It should be noted that in this phase, the crystallographic a and c directions are interchanged relative to phase II [see Fig. 2(c)], resulting in an equivalent view of the molecular stacking. Despite the emergence of new symmetries (only those concerning the $2_1/n$ perpendicular to the b axes remain in both phases), such as the mirror m (perpendicular to the c axes), the stacking and the in-plane disorder remain virtually unchanged [see Figs. 2(c) and 2(d)]. The molecules occupy two different sites, with occupational factors of 0.5 each (which actually originates the mirror). We attempted a refinement with the molecule placed exactly on the mirror plane, but the result was significantly worse. Such a structural result could be associated with a dynamic "swinging" of the molecules that the space-time average captured by x-ray diffraction cannot resolve. Through the molecular dynamics simulations (see later), such a movement, together with the dynamic correlations between adjacent molecules, will be described.

Lattice parameters as a function of temperature for phase I are also gathered in Table S3 (Supplemental Material [33]). For ease of comparison between the structures of both phases, as well as for analyzing the temperature dependence of the lattice parameters, the a and c axes of phase I have been interchanged.

The features of the measured thermal effect (inset of Fig. 1), as well as the group–subgroup relationship between phases II and I ($P2_1/n \rightarrow Pnnm$), indicate the occurrence of a second-order phase transition. To highlight the continuous nature of the II–I phase transition, we have constructed an order parameter (OP) on the basis of the crystallographic data, defined as

$$\mathrm{OP}(T) = \frac{b(T)\cos[\beta(T)]}{b(0)\cos[\beta(0)]}, \tag{1}$$

where $\beta(0)$ and $b(0)$ are the values of the lattice parameters extrapolated to 0 K.

Figure 4 shows the variation of the OP with temperature. This quantity decreases smoothly with increasing temperature

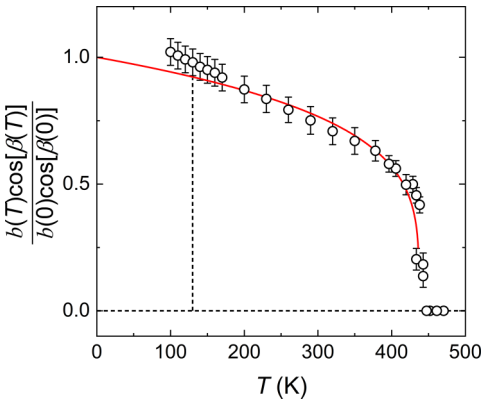

FIG. 4. Temperature dependence of the order parameter defined according to Eq. (1). The order parameter vanishes when $\beta = 90^\circ$, indicating a symmetry increase in the crystal lattice. A sharp drop to zero is observed at 437 K, consistent with a second-order group–subgroup phase transition. Vertical dashed line indicates the glass transition temperature (see Fig. S1 of Supplemental Material [33]).

and vanishes at the transition point when $\beta = 90^\circ$, indicating the symmetry increase of the crystal lattice. As shown in Fig. 4, the OP follows a power-law behavior that can be expressed as

$$\mathrm{OP}(T) = \left(1 - \frac{T}{T_{\mathrm{II-I}}}\right)^{\gamma}, \tag{2}$$

where $T_{\mathrm{II-I}}$ is the transition temperature and γ is a critical exponent. A fit of Eq. (2) within the temperature range between the glass transition temperature (see Fig. S1 in the Supplemental Material [33]) and the phase transition yields $\gamma = 0.229$, which is close to critical exponents found for molecular systems [21,22].

C. Quasielastic neutron scattering

To follow the evolution of molecular dynamics across the continuous II → I phase transition, it is essential to monitor how characteristic timescales vary over a broad temperature interval. In a second order phase transition the overall mechanism should remain unchanged, i.e., no sudden change is expected, for this reason we have investigated the dynamics over a large temperature that extends tens of Kelvins. To capture this gradual evolution, preliminary scans measurements were performed on both instruments: an EWS on OSIRIS and combined elastic and inelastic FWS on IN16B. These measurements provide a rapid overview of the temperature dependence of the elastic and inelastic intensities, enabling the identification of the onset of motion within the instrumental time window and guiding the selection of temperatures for full spectral analysis. In addition, the scans performed on IN16B allow an initial, qualitative estimation of the activation behavior of the dominant relaxation process.

The EWS collected on OSIRIS monitors the integrated intensity of the elastic peak within the instrumental resolution limits, as described in the Methods section.

Above ca 400 K, the observed nonmonotonic decrease in the elastic intensity relative to lower temperatures, as shown in Fig. 5(a), indicates that molecular reorientations gradually enter the OSIRIS time window as the system approaches phase I.

On IN16B, FWS were performed by monitoring the intensity at three selected energy transfers: $E = 0$ μeV (EFWS) and $E = 3$ and 6 μeV (IFWS). The resulting curves [Fig. 5(b)], recorded between 5 and 462 K, reveal several distinctive features. First, the EFWS signal decreases continuously with increasing temperature, while the IFWS intensities exhibit a clear maximum, reflecting the redistribution of spectral weight from elastic to inelastic channels as the existing reorientational dynamics enter within the time windows of the instrument. A notable change in the slope of the inelastic intensity occurs near 437 K, in agreement with the DSC anomaly marking the II → I phase transition.

An additional feature is observed at very low temperatures: the EFWS shows an initial drop accompanied by a peak in the IFWS curves, which do not start from zero at the lowest

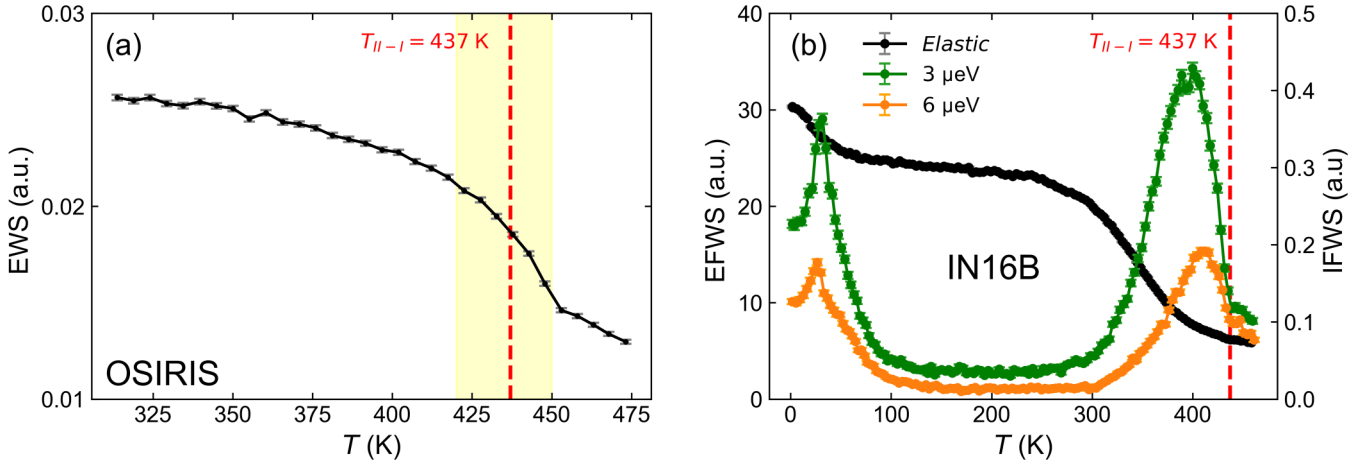

FIG. 5. Temperature dependence of the elastic and inelastic fixed-window intensities. (a) EWS from OSIRIS, showing the integrated elastic intensity within the instrumental resolution as a function of temperature during heating. (b) FWS from IN16B, displaying the elastic signal (EFWS) at $E = 0$ μeV (left axis—black circles) and the inelastic intensities (IFWS) at $E = 3$ and 6 μeV (right axis—green and orange circles, respectively) over the range 5–462 K. The vertical dashed red line marks the transition temperature obtained by DSC.

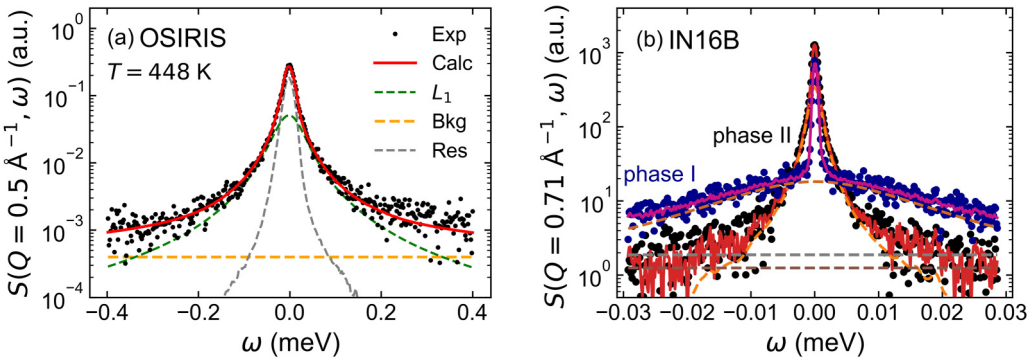

FIG. 6. QENS spectra of TCMX at selected temperatures in phase II and phase I, measured on OSIRIS and IN16B spectrometers. (a) OSIRIS spectrum at $T = 448$ K showing the experimental data (symbols), total fit (solid red line), instrumental resolution (dashed gray line), and individual components: Lorentzian (dashed green line) and flat background (dashed orange line). (b) IN16B spectra in phase II ($T = 365$ K) and phase I ($T = 440$ K), highlighting the clear difference in linewidth between the two phases. Experimental data are shown as symbols, with the corresponding total fit in solid lines. Individual fit components (lorenzian and flat background) are represented by dashed lines.

temperatures. Since this behavior appears far below the glass transition temperature ($T_g \approx 128$ K; see Fig. S1 of the Supplemental Material [33]), it is tentatively attributed to quantum tunneling of methyl groups, i.e., hydrogen atoms undergoing rotational tunneling at cryogenic temperatures [50,51]. The peak observed between 0 and 100 K likely marks the crossover from quantum rotation to thermally activated classical rotation.

Overall, the evolution of elastic and inelastic intensities across the entire temperature range confirms the absence of abrupt dynamical changes, consistent with a continuous transition. These scans also provide a basis for selecting representative temperatures for high-statistics quasielastic spectra in both phases and across the transition region.

To analyze the quasielastic spectra, we describe the dynamic structure factor as the sum of an elastic component and one or more Lorentzian functions accounting for relaxation processes:

$$S_{\text{theor}}(Q,\omega) = A_0(Q)\,\delta(\omega) + \sum_{i=1}^{n} A_i(Q)\,\frac{1}{\pi}\left(\frac{\Gamma_i}{\omega^2+\Gamma_i^2}\right), \quad (3)$$

where $A_0(Q)$ is the elastic intensity, and each Lorentzian is characterized by its half-width at half-maximum Γ_i and amplitude $A_i(Q)$.

The experimental spectra are related to the theoretical function by convolution with the instrumental resolution $R(Q,\omega)$:

$$S_{\text{obs}}(Q,\omega) = R(Q,\omega) \otimes S_{\text{theor}}(Q,\omega). \quad (4)$$

Following the model selection analysis (see Sec. II of the Supplemental Material [33]) and the identification of representative temperatures for each instrument (see Methods), the QENS spectra were analyzed using a model consisting of one Lorentzian term plus a flat background. For each chosen temperature, the spectra were examined as a function of momentum transfer Q to account for possible Q-dependencies of the parameters of the dynamical process.

Special care was taken to minimize the contribution of coherent scattering. The first Bragg peak, identified from the diffraction patterns at $Q \approx 0.8{-}0.9$ Å^{-1}, was avoided in the fitting procedure. For OSIRIS, analysis was restricted to groups of equispaced Q values between 0.3 and 0.8 Å^{-1}, just below the first diffraction peak, ensuring that the spectra primarily reflected the incoherent contribution. For IN16B, a masking procedure was applied to remove the Bragg peak region without truncating the remainder of the spectrum.

The fitting was performed at each Q using the Lorentzian + flat background model convoluted with the resolution function. Figure 6 shows representative examples of the experimental spectra and their corresponding fits. Figure 6(a) shows an OSIRIS spectrum at $T = 448$ K for a selected Q value within the incoherent region ($Q = 0.5$ Å^{-1}), together with the total fit, the instrumental resolution, and the individual components (Lorentzian and background). Figure 6(b) displays IN16B spectra collected at two temperatures representative of phase II and phase I. The higher resolution of IN16B allows a clearer observation in linewidth difference between the two phases, revealing the progressive broadening of the quasielastic signal as the temperature increases. In both instruments, the chosen model provides an excellent description of the data, confirming the dominance of a single relaxation process across the transition.

The Lorentzian linewidths (Γ) obtained from the fits were converted into characteristic times using the relation $\tau = \hbar/\Gamma$. This time represents the timescale of the dominant collective reorientational process in TCMX. Figure 7 displays the resulting values in an Arrhenius plot ($\log(\tau)$ versus $1000/T$), combining the results from both OSIRIS and IN16B instruments.

The two datasets define a single linear trend across the entire temperature range, indicating that the activation energy, E_a, remains essentially constant through the II → I phase transition. This behavior confirms that the underlying molecular mechanism does not change between phases. A slight (but detectable) vertical offset between the two phases reflects the influence of the symmetry change on the rotational potential, without altering the fundamental nature of the motion.

The geometry of the reorientational motion was further examined through the elastic incoherent structure factor (EISF), given by the amplitude of the elastic signal $A_0(Q)$. EISF is

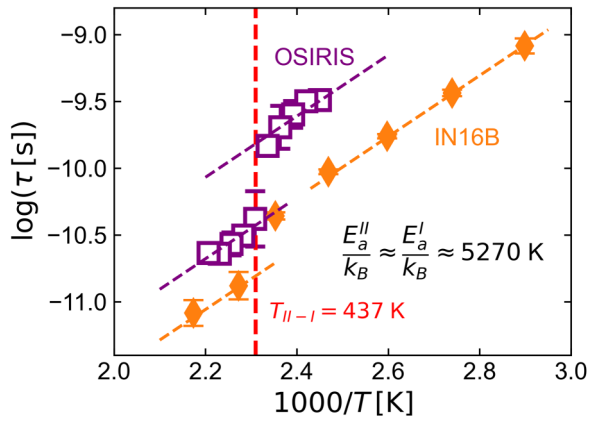

FIG. 7. Arrhenius plot of the characteristic relaxation time τ as a function of the reciprocal temperature $(1000/T)$ for TCMX, obtained from fittings of the QENS spectra. Data from OSIRIS (purple symbols) and IN16B (orange symbols) define a common linear trend, indicating that the activation energy remains essentially constant across the II → I phase transition (vertical dashed red line).

commonly defined as the ratio of the elastic intensity to the total scattered intensity [Eq. (5)]:

$$\mathrm{EISF}(Q) = \frac{I_{\mathrm{elastic}}}{I_{\mathrm{elastic}} + I_{\mathrm{inelastic}}}. \tag{5}$$

Unlike the quasielastic linewidth, which reflects the timescale of motion, the EISF provides insight into the spatial characteristics of the dynamics. Figure 8(a) shows the EISF as a function of Q for IN16B data at different temperatures.

The experimental points were fitted using a six-site jump model, consistent with the six-fold rotational symmetry of the TCMX molecule. The fits reproduce the experimental data across the entire Q range, confirming that the dominant process corresponds to discrete jumps among symmetry-equivalent orientations.

Figure 8(b) displays the effective rotation radius r extracted from these fits as a function of temperature. For phase II at 365 K, the fitted radius is $r = 3.56 \pm 0.11$ Å, while for phase I at 440 K it increases slightly to $r = 4.40 \pm 0.12$ Å. The clear jump in r with temperature might imply additional rattling of the molecular center-of-mass and, therefore, a larger effective rotational radius. Intermediate temperatures follow a smooth trend between these values. The fact that a detectable increase in r appears slightly below the transition temperature reflects pretransitional effects, which are expected in continuous high-order transitions and naturally extend into the low-temperature phase. Such behavior does not indicate a shift in the transition temperature, but rather the progressive softening of the rotational potential upon heating. These distances are fully compatible with size of the TCMX molecule, further supporting the interpretation of rotational jumps around the sixfold axes perpendicular to the molecular plane. The nearly constant geometry across the transition reinforces that the symmetry change between II and I does not alter the nature of the motion, but only affects its timescale.

To gain further insight into the microscopic origin of this transition and to understand how orientational correlations evolve across phases, we turn next to molecular dynamics simulations.

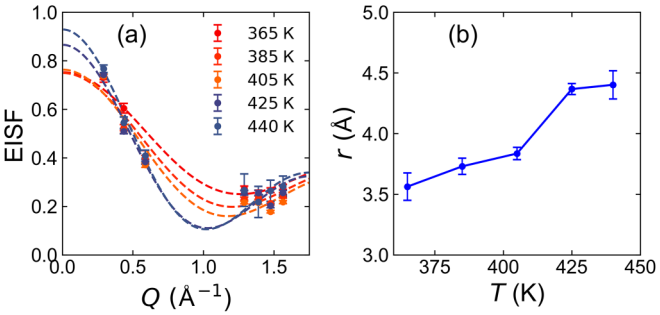

FIG. 8. (a) Elastic incoherent structure factor (EISF) of TCMX as a function of Q, measured on IN16B at different temperatures. Dashed lines correspond to the fits using a six-site jump model, consistent with the molecular symmetry. (b) Effective rotation radius r extracted from the fits at different temperatures.

D. MD simulation

MD simulations are particularly well suited to investigate subtle phase transitions like this one. They provide microscopic access to structural and dynamical details that are inaccessible to diffraction methods, which yield only time-averaged information [26,52]. We have performed a set of MD simulations in the NPT (i.e., fixed number of particles, N, pressure P, and temperature, T) ensemble to provide a microscopic description of the phase transition experimentally observed in TCMX. The MD simulations reproduce a phase transition, reflected in a change of specific volume, in good agreement with the experimental results: as shown in Fig. 9, there is an increase in volume, resulting in a 0.6% expansion, when extrapolating the volume of high and low temperature phase to the transition temperature. Despite the subtlety of the effect, both experimentally and in the simulations, the transition is clearly detectable, which demonstrates the reliability of our simulations.

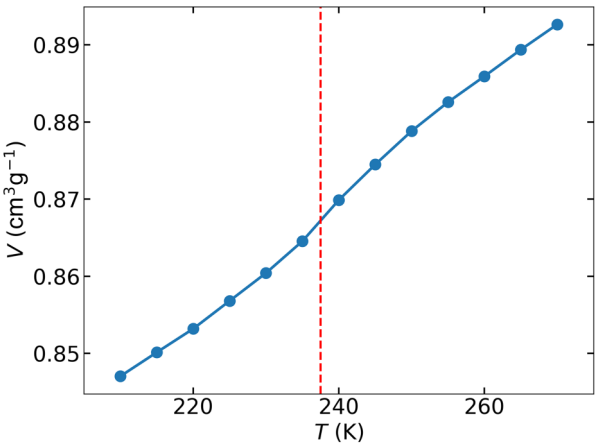

FIG. 9. Volume evolution of TCMX as a function of temperature, obtained from constant-pressure (NPT) molecular dynamics simulations. The phase transition appears as a kink in the volume curve around $T_{\mathrm{II\text{-}I}}^{\mathrm{sim}} = 235$ K, indicated by the dashed vertical red line. The solid line is included as a guide to the eye.

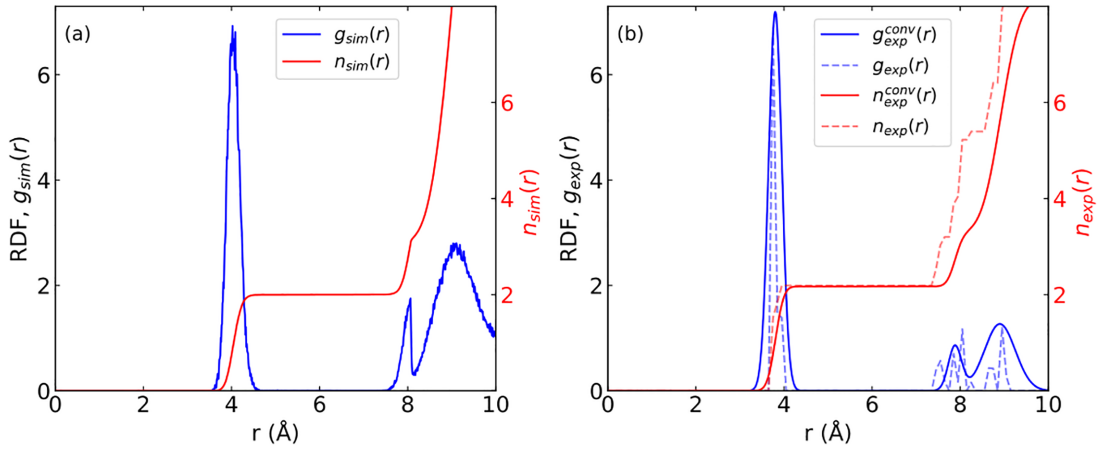

FIG. 10. Radial distribution function $g(r)$ (blue) and the cumulative coordination number $n(r)$ (red) of TCMX as a function of the distance from the centers of the carbon ring. (a) Results obtained from constant-pressure molecular dynamics (NPT-MD) simulations for the low-temperature phase II. (b) Experimental results: the dashed lines correspond to the $g(r)$ and $n(r)$ computed directly from the crystal structure obtained by diffraction data, while the solid lines show the Gaussian-convoluted curves that mimic the effect of thermal agitation.

The transition temperature predicted by our simulations ($T^{\text{sim}}_{\text{II-I}} = 235\,\text{K}$) does not match the experimental value ($T^{\text{exp}}_{\text{II-I}} = 437\,\text{K}$). This discrepancy is most likely related to the limitations of the employed force field, which may not fully capture the balance of intermolecular interactions responsible for stabilizing the different phases. Such deviations in the absolute transition temperature are relatively common in molecular dynamics simulations of molecular crystals and highlight the sensitivity of phase-transition predictions to the parametrization of the potential model, as reported in previous simulation studies on polymers [53–55]. Nevertheless, as we will show in the following sections, other structural and thermodynamic properties associated with the transition are correctly reproduced by the simulations, supporting the validity of the microscopic picture provided by our calculations.

To further validate the accuracy of our simulations, we calculate the radial distribution function (RDF), $g(r)$, between the centers of the carbon ring for phase II and compare it with the experimental results obtained from the structure of the diffraction data. The simulated RDF is shown in Fig. 10(a), displaying three well-defined peaks that correspond to distinct coordination shells. In addition to the RDF, we also show the cumulative coordination number $n(r)$, which provides complementary insight into how many neighboring molecules are contained within a given radial distance. The first steep increase in $n(r)$ confirms that the first peak of RDF corresponds to the two nearest neighbors, in agreement with the expected local coordination in phase II.

Figure 10(b) shows the experimental RDF, derived directly from the diffraction measurements (dashed line), together with its corresponding $n(r)$. The solid curves represent the Gaussian-convoluted profiles, introduced to mimic the effect of thermal agitation and enable a clearer comparison with the simulation results.

The discrepancy between the simulated and experimental RDFs arises from the way thermal motion is treated in each case. The crystal structure obtained by diffraction, via Rietveld refinement, represents average atomic positions over time, corresponding to what in molecular dynamics would be considered *intrinsic structures*. As a result, the RDF derived directly from this structure lacks the broadening associated with thermal fluctuations. To account for this, we convolute the experimental RDF with Gaussian functions, effectively mimicking the effect of thermal agitation. The resulting convoluted RDF is shown as a solid line in Fig. 10(b). The excellent agreement with the simulation confirms that the structural features observed in the MD trajectories are consistent with the experimental data.

To clarify the origin of the three peaks observed in the simulated RDF, we analyze the molecular arrangement within the crystal lattice. This lattice has been generated directly from the atomic positions arising from experimental x-ray results and reflects the actual crystal structure. From the figure, it is evident that the structure is defined by well-organized molecular stacking columns. After direct inspection of the obtained lattice, the first peak of the RDF corresponds to the nearest-neighbor molecules located directly above or below a reference molecule within the same stacking column.

The assignment of the second and third peaks requires further consideration: due to the crystal geometry, the distance to the second-nearest neighbor along the same column and the distance to the closest molecule in an adjacent column are similar, making a clear distinction nontrivial.

We tentatively assign the sharp second peak to the next-nearest neighbor within the same stacking column, which appears at approximately twice the distance of the first peak, consistent with its more defined nature. The broader third peak is attributed to the closest neighbors belonging to adjacent stacking columns. This tentative interpretation will be verified by analyzing the relative positions and orientations of neighboring molecules in a subsequent section.

Our results thus indicate that the employed force field in the molecular dynamics simulations reliably reproduces the features observed experimentally. This provides a solid basis to investigate the subtle changes that must occur during the phase transition. To this end, we will analyze the orientations of the TCMX molecules from two distinct, yet complementary, perspectives:

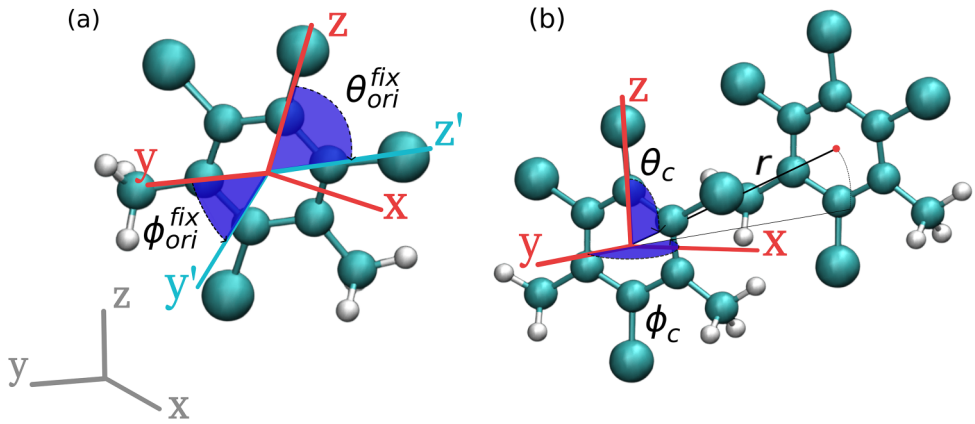

FIG. 11. Schematic representation of the orientational and positional angles used in this study. The red axes in both panels define the molecular coordinate system attached to each TCMX molecule. (a) The fixed crystallographic frame (in gray) enables the definition of the angles that describe the orientation of a TCMX molecule with respect to the crystal lattice. (b) Definition of the angles used to calculate the relative position and orientation between molecules. Two sets of angular coordinates are defined: (θ_c, ϕ_c) describe the position of a neighboring molecule's center of mass, while $(\theta_{ori}^{fix}, \phi_{ori}^{fix}, \psi_{ori}^{fix})$ are the Euler angles defining its orientation relative to the reference molecule.

(1) First, we will examine the possible orientations of the molecules with respect to a *fixed axes* attached to the crystal lattice (a so called laboratory reference frame).

(2) Second, to assess whether the phase transition is merely associated with a collective reorientation of all molecules or also involves changes in the correlation between neighboring molecules, we will study the orientation of one molecule relative to another, i.e., as seen from a comobile axes set attached to each molecule.

It is important to clarify that this type of analysis cannot be performed using x-ray experiments, since the molecules are effectively superimposed on each other and no relative positions can be resolved. This combined approach will enable us to characterize both the global orientational behavior and the local correlation patterns that define this disorder-disorder phase transition. In both cases, a molecular coordinate system attached to TCMX molecule must first be defined.

As illustrated in Fig. 11(a), we assign to each molecule of TCMX a molecular coordinate frame (shown in red), centered at the center of the benzene ring. The z axis is defined along the vector pointing from the center of the benzene ring to the chlorine (Cl) atom, oriented opposite to the direction of the two methyl groups (CH_3). The x axis is set along the vector connecting the center of the ring to the midpoint between two carbon atoms on the aromatic ring. The y axis is defined as perpendicular to the zx plane, completing a right-handed orthonormal coordinate system. This comobile molecular coordinate system is rigidly attached to each TCMX molecule and defines its orientation with respect to either a fixed or comobile molecular axis throughout the analyzed configurations.

1. Molecular orientations with respect to the crystal lattice

We begin by analyzing the orientation of individual TCMX molecules in both phases with respect to the crystallographic axes. Based on the molecular coordinate frame defined above, we compute the Euler angles θ_{ori}^{fix} and ϕ_{ori}^{fix} relative to the crystallographic axes shown in Fig. 11(a) (in gray). These angles follow standard polar and Euler conventions and provide a quantitative description of the molecule's orientation throughout the simulation. Specifically, θ_{ori}^{fix} is associated with the rotation of the ring around an axis perpendicular to its plane, while ϕ_{ori}^{fix} corresponds to the tilt of the ring with respect to the crystallographic axes.

The angle θ_{ori}^{fix} captures molecular rotations around the crystallographic axes aligned with the stacking direction of the TCMX columns. In contrast, ϕ_{ori}^{fix} is directly related to the tilt of the aromatic ring plane. As illustrated in Fig. 12(c), this tilt depends on the stacking column to which the molecule belongs: molecules within the same column adopt the same tilt angle. This angular decomposition is particularly well suited to identify reorientational signatures associated with the phase transition.

To determine whether molecular orientation with respect to a fixed crystallographic axes changes across the phase transition, we compute the two-dimensional probability distribution function of the angular coordinates (angular maps) ϕ_{ori}^{fix} and $\cos(\theta_{ori}^{fix})$, as shown in Figs. 12(a) and 12(b).

The compensation for the nonuniform solid angle associated with spherical coordinates is done by representing in the horizontal axes the cosine of the azimuthal angle $\cos(\theta_{ori}^{fix})$, ensuring uniform binning across the entire angular range.

In this map, each localized spot corresponds to a distinct orientation of the TCMX molecular ring with respect to the fixed crystallographic axes. To ensure that the simulation does not artificially distort the orientational structure (or produce configurations incompatible with experiment) we also plot, as red dots in Fig. 12(a), the same angular distribution extracted directly from the diffraction experiment. The red points align closely with the simulated spots obtained after equilibration, suggesting that the force field used for the simulation accurately captures the main features of the experimentally observed orientational order.

Figures 12(a) and 12(b) show a series of well-defined spots distributed along both angular axes. Each spot corresponds to a frequent orientation adopted by the TCMX molecule in the crystal. To interpret the meaning of these spots, we recall the

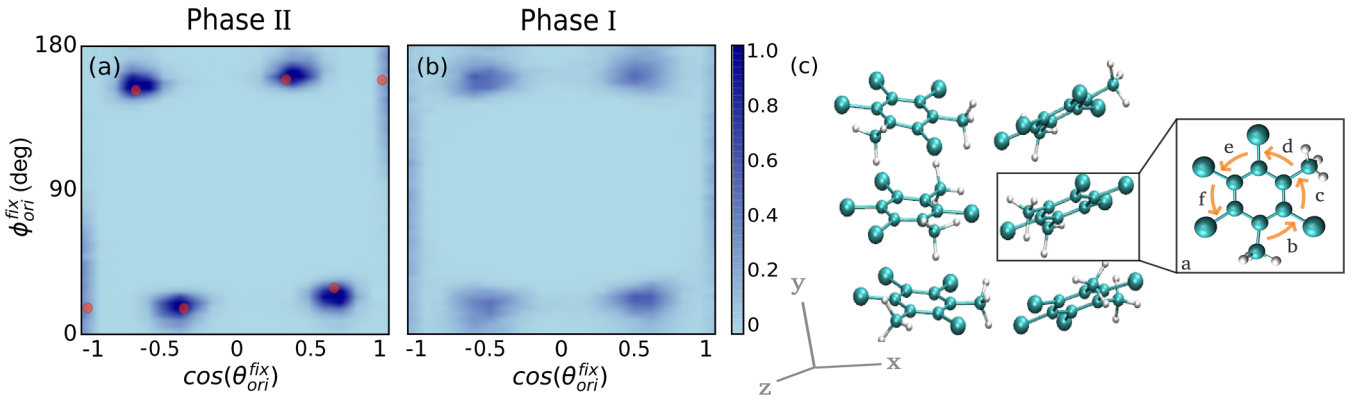

FIG. 12. Two-dimensional probability distribution functions of the angles $\phi_{\rm ori}$ and $\theta_{\rm ori}$ defining the orientation of a TCMX molecule with respect to the crystallographic axes: (a) before the transition at $T = 210$ K, and (b) after the transition at $T = 270$ K. The red points represent data extracted from the 3D crystal structure obtained from diffraction measurements. (c) Snapshot from the MD simulation. Two types of stacking can be clearly identified, each associated with a different tilt angle $\phi_{\rm ori}$. As an inset, we show the ring orientations that TCMX molecules can adopt by rotating around the axis perpendicular to the ring (labeled from a to f), as defined by angle $\theta_{\rm ori}$.

geometric definitions of the angles $\theta_{\rm ori}^{\rm fix}$ and $\phi_{\rm ori}^{\rm fix}$ introduced in Fig. 11(a). The angle $\phi_{\rm ori}^{\rm fix}$ quantifies the orientation of the axis perpendicular to the molecular ring with respect to the crystallographic frame (tilt angle). Since molecules in the same stacking column share the same tilt angle, all spots aligned horizontally (i.e., with the same $\phi_{\rm ori}^{\rm fix}$) are attributed to the same stacking.

Along each horizontal row, four distinct values of $\cos(\theta_{\rm ori}^{\rm fix})$ are observed: two near ±1 and two near ±0.5 (regardless of the $\phi_{\rm ori}^{\rm fix}$ angle), corresponding approximately to molecular orientations at 0°, 60°, 120°, and 180° with respect to the ring normal. These discrete values reflect the sixfold symmetry of the molecule due to the rotational in-plane disorder. However, due to the cosine projection, the $\pm60°$ and $\pm120°$ orientations yield identical $\cos(\theta_{\rm ori}^{\rm fix})$ values, reducing the six possibilities to four visible spots (ring orientations) per stacking.

The first evident difference between the two phases lies in the size and sharpness of the spots observed in Figs. 12(a) and 12(b): at high temperature, the distributions are noticeably broader and, consequently, less defined, reflecting the increased thermal agitation, in line with larger effective rotational radius inferred from QENS [Fig. 8(b)].

More interestingly, the positions of the spots remain almost unchanged between the low- and high-temperature phases. This indicates, as expected from both diffraction data and the continuous variation of volume through the phase transition, that the structural differences between the two phases are subtle and do not involve large changes in the orientation of the molecules with respect to the fixed crystallographic axes.

A closer inspection, however, reveals a significant and informative detail. In the high-temperature phase I, the spots are distributed at angular intervals of precisely 60° in $\theta_{\rm ori}^{\rm fix}$, reflecting perfect sixfold rotational symmetry around the axis perpendicular to the molecular ring. This implies that all molecules, regardless of the stacking column to which they belong (i.e., their $\phi_{\rm ori}^{\rm fix}$ value), can adopt any of the six symmetry-equivalent orientations.

In contrast, in the low-temperature phase the spots are no longer located exactly at $\theta_{\rm ori}^{\rm fix} = 0°$, 60°, 120°, and 180°, but appear slightly shifted (either above or below these ideal angles) depending on the stacking index (i.e., the value of $\phi_{\rm ori}^{\rm fix}$). Since $\phi_{\rm ori}^{\rm fix}$ identifies the stacking column, this systematic deviation in $\theta_{\rm ori}^{\rm fix}$ suggests the presence of interstacking orientational interactions, preventing molecules in different columns from adopting exactly the same orientation of the ring, with respect to the stacking axes. Instead, they are slightly rotated (either ahead of or behind) the equilibrium angles characteristic of the high-temperature phase.

This observation supports the interpretation that the high-temperature phase is more symmetric, while the low-temperature phase develops subtle orientational correlations between neighboring columns, leading to a symmetry-breaking consistent with the experimental evidence. To quantify how the orientation of the rings of TCMX molecules varies between different stackings, we analysed the values of $\cos(\theta_{\rm ori}^{\rm fix})$ corresponding to spots located at similar angular positions across stackings. Specifically, for each of the

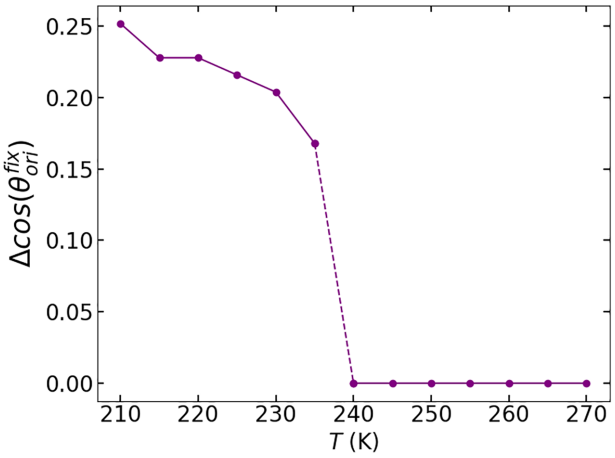

FIG. 13. Differences in the orientation of the ring with respect to the crystallographic axes: $\Delta\cos(\theta_{\rm ori}^{\rm fix}) = \cos(\theta_{i,\rm ori}^{\rm fix}) - \cos(\theta_{j,\rm ori}^{\rm fix})$ as a function of temperature. A drop to zero is observed at the transition temperature.

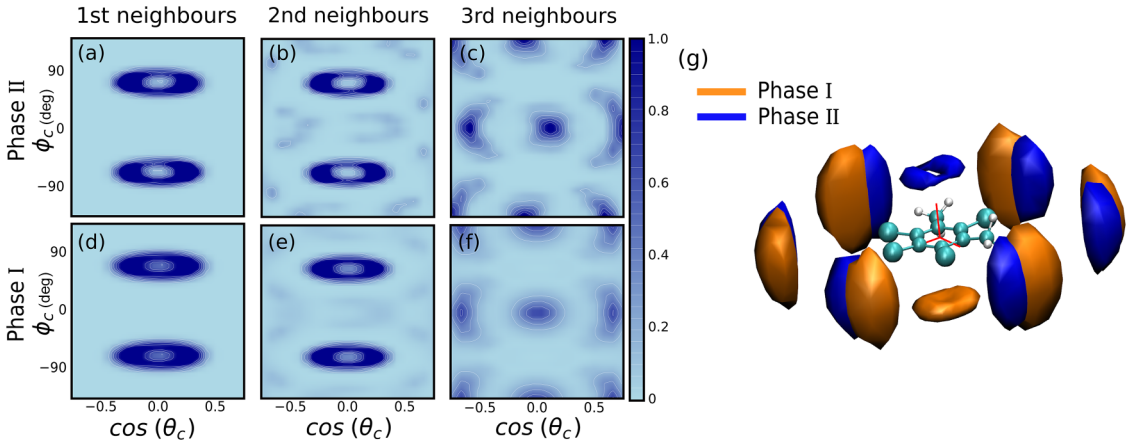

FIG. 14. Angular maps of ϕ_c and $\cos(\theta_c)$ for neighboring molecules, showing the relative position of two TCMX molecules. Panels (a)–(c) correspond to the low-temperature phase II while panels (d)–(f), to the high-temperature phase I. The columns show the maps for first (a), (d), second (b), (e), and third (c), (f) neighbors. Panel (g) shows a representation of the surface positions of the first (upper and lower torus) and third neighbors (lobes in the plane of the ring), corresponding to the low-temperature phase II (blue) and the high temperature phase I (orange). For clarity, only one of the two positions for first neighbors is shown, as they are very similar. Red axes indicate the molecular coordinate frame.

characteristic orientations found in the high-temperature phase (at 0°, 60°, 120°, and 180°), we identified all corresponding spots at different values of $\phi_{\text{ori}}^{\text{fix}}$, that is, from different stacking columns, and computed the pairwise differences in $\cos(\theta_{\text{ori}}^{\text{fix}})$. We then averaged these differences to obtain a global overview of the orientational mismatch between stackings at each temperature. The resulting quantity, $\Delta\theta_{\text{max}}$, is shown in Fig. 13.

As seen in that figure, $\Delta\cos(\theta_{\text{ori}}^{\text{fix}})$ decreases with increasing temperature and drops sharply to zero at the transition point. This indicates that above the transition, molecules in different stackings adopt identical orientations, consistent with a higher-symmetry phase. Below the transition, however, small but systematic deviations of the rotation of the ring appear between stackings, reflecting the onset of interstacking orientational correlations.

This behavior is fully consistent with the structural interpretation derived from both simulation and experiment. The continuous vanishing of orientational differences at the transition confirms that the high-temperature phase is more symmetric, while the low-temperature phase exhibits interstacking constraints that slightly distort the ideal angular configurations.

2. *Molecular orientations with respect to the molecular mobile system*

In the previous section we saw that molecules in different stacking columns show different ring orientations. Now we want to answer two questions:

(1) Does the relative *position* of one TCMX molecule with respect to another change across the transition? This position is defined by the spherical angles θ_{cm} and ϕ_{cm}, which, as shown in Fig. 11, indicate the location of a neighboring molecule's center of mass relative to a central reference molecule using its comobile frame.

(2) Does their *orientation* relative to each other also change? This is described by the Euler angles θ_{ori}, ϕ_{ori}, and ψ_{ori}, which quantify the relative orientation of a neighboring molecule with respect to the comobile frame of the reference molecule.

We begin with the positional part, characterized by θ_{cm} and ϕ_{cm}. First, we build the probability map of the center-of-mass (CM) position of a TCMX molecule around a reference molecule. We do this for the first, second, and third neighbor shells, defined by the three peaks of the radial distribution function $g(r)$ (Fig. 10). The maps for the first and second shells are almost identical. This tells us that the second peak appearing in $g(r)$ simply comes from molecules in the *same* stacking column but at twice the distance, as tentatively stated in the previous section.

The third shell is different. Although a direct interpretation of the map in (Fig. 14) is not easy, the three-dimensional reconstruction in Fig. 14(c) [the spatial density map (SDM)] makes its meaning obvious. Here the most probable location of the center of the ring of the first neighbors appear just above and below the reference molecule, along the column axes, while the third neighbors form side lobes in the plane of the ring. This shows that third neighbors belong to a different column. Because the reconstruction averages over all molecular orientations, six lobes of high probability appear, reflecting the six possible relative arrangements produced by 60° rotations of the TCMX ring.

We begin by analyzing the relative positions of first-neighbor molecules, i.e., those belonging to the same stacking column. As shown in Fig. 14, the angular distribution forms a toroidal shape at both low and high temperatures. This indicates that the center of mass of a neighboring molecule is not located exactly along the axis perpendicular to the ring and passing through the center of mass of the central molecule, but slightly offset. The exact position depends on the rotational state of both molecules.

Importantly, the shape and position of this torus are essentially the same in both phases. At high temperature the torus appears slightly thicker, due to thermal agitation, but its overall structure remains unchanged. This suggests that the phase

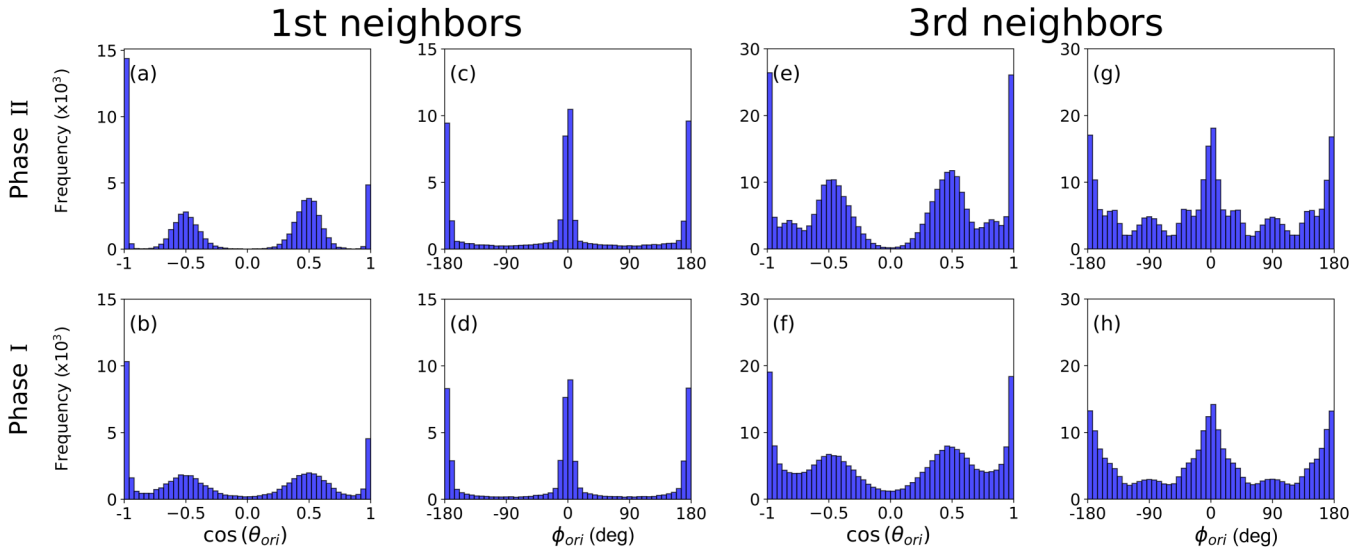

FIG. 15. One-dimensional histograms of $\cos(\theta_{\rm ori})$ (a), (b), (e), (f) and $\phi_{\rm ori}$ (c), (d), (g), (h) for first neighbors (intra-column interaction), panels (a)–(d), and the third neighbors (intercolumn interaction), panels (e)–(h). The first row corresponds to the low-temperature phase II, while the second row corresponds to the high-temperature phase I.

transition does not affect the positional correlation between molecules within the same stacking. The reconstructed SDMs shown in Fig. 14(c) confirm this interpretation: the torus representing first-neighbor positions remains well-defined in both phases. The SDM also shows that these neighbors are never located exactly along the molecular axes of the central molecule, but are always slightly displaced. High and low temperature results are plotted in different colours to facilitate direct comparison.

In contrast, the behavior of third-neighbor molecules (those belonging to adjacent stacking columns) is markedly different. In Fig. 14, the general shape of the angular distribution is again similar in both phases, as in the orientation analysis with respect to a fixed axes. However, a systematic displacement of the spots is (again) observed. Although this angular map contains all the necessary information to reconstruct the relative positions, its interpretation is not straightforward. It is difficult to visualise what the angular distribution implies about the actual position of the neighboring molecule. For this reason, we turn again to the SDM shown in Fig. 14(c).

In high-temperature phase I (orange lobes), third-neighbor molecules occupy positions separated by precise 60° intervals, consistent with the fixed-axes analysis that showed all molecules (regardless of stacking) adopting the same set of orientations. This reflects the high-symmetry character of the disordered phase. In the low-temperature phase II (blue lobes), however, these positions no longer coincide with the high-temperature reference. The lobes are slightly rotated away from the symmetric values. This confirms our earlier hypothesis: molecules in different stackings no longer adopt exactly the same equilibrium orientations. Instead, they are slightly shifted from one stacking to another, likely as a result of steric interactions.

To complete the analysis, we now focus on the relative orientation between neighboring molecules. This is characterized by the three Euler angles $\theta_{\rm ori}$, $\phi_{\rm ori}$, and $\psi_{\rm ori}$, which describe the rotation required to align the comobile frame of one molecule with that of a neighbor. Due to the symmetry of the molecule combined with that of the crystalline lattice, the angles $\phi_{\rm ori}$ and $\psi_{\rm ori}$ are equivalent. For this reason, we focus our attention on the angles $\theta_{\rm ori}$ and $\phi_{\rm ori}$.

The angle $\theta_{\rm ori}$ describes the relative rotation of the aromatic ring around a perpendicular axis between two molecules. In contrast, the angle $\phi_{\rm ori}$ represents the tilt between the planes of the two molecules, capturing how their ring normals are oriented relative to each other.

In Fig. 15, we show the histograms of $\theta_{\rm ori}$ and $\phi_{\rm ori}$ for molecular pairs corresponding to the first and third peaks in the radial distribution function $g(r)$, that is, for nearest neighbors within the same stacking column, and in adjacent columns.

For first neighbors, Figs. 15(a)–15(d) show no significant differences between the low- and high-temperature phases for either angle. This indicates that the relative orientation (both in terms of ring rotation and tilt) remains unchanged for molecules in the same column.

The situation is very different for molecular pairs belonging to different stackings [Figs. 15(e)–15(h)]. In this case, additional peaks appear in the angular distributions of both $\theta_{\rm ori}$ and $\phi_{\rm ori}$ in the low-temperature phase, indicating that molecules in adjacent columns interact differently in the two phases. From a general point of view, we can state that the number of distinct orientations increases in the low-temperature phase, reflecting a reduction in symmetry. This observation is fully consistent with the rest of the analysis presented in this work.

We now turn to the physical interpretation of the additional peaks observed in the low-temperature phase.

(1) For the angle $\theta_{\rm ori}$, which governs the relative in-plane orientation between two TCMX molecules, an additional peak emerges at approximately $\theta_{\rm ori} \approx 30°$. This value lies between the fully parallel configuration and the next equilibrium

orientation at $\theta_{\text{ori}} = 60^\circ$, suggesting the presence of intermediate rotational states between the stable orientations.

(2) For the tilt angle ϕ_{ori}, additional peaks appear close to $\phi_{\text{ori}} = \pm 180^\circ$ and $\phi_{\text{ori}} = 0^\circ$. These features indicate that molecules in adjacent columns preferentially adopt orientations that deviate from the equilibrium configurations.

Taken together, these observations point to a steric interaction between molecules in different columns, which restricts their accessible configurational space and promotes intermediate orientations involving both a modest tilt (approximately 20°) and a partial rotation (approximately 30°).

The whole analysis leads to a key conclusion: the microscopic origin of the phase transition lies in the interaction between molecules from different stackings. In the low-temperature phase, the distance between columns is smaller, and steric hindrance prevents all molecules from adopting identical orientations. Each column adjusts slightly to avoid overlap. In the high-temperature phase, the columns are farther apart, allowing all molecules to adopt the same configuration independently of stacking. This restoration of symmetry is fully consistent with the experimental diffraction results.

IV. CONCLUSIONS

We have identified a previously unreported high-temperature phase transition in TCMX at approximately 437 K, corresponding to a continuous, second-order group-subgroup transformation between two orientationally disordered crystalline phases. The transition was first detected through a weak but reproducible thermal anomaly in differential scanning calorimetry, and confirmed structurally via temperature-dependent x-ray diffraction, which reveals a symmetry increase without major structural reconstruction.

To understand the microscopic origin of this subtle transformation, we combined structural and dynamical experimental probes with molecular dynamics simulations. Quasielastic neutron scattering measurements show that reorientational dynamics, discrete 60° molecular jumps, persist across the transition with no significant change in activation energy or geometry. The simulations reproduce the transition and reveal that the low-temperature phase exhibits weak intercolumnar orientational correlations, which are lost in the high-temperature phase. Altogether, our results establish that the transition is driven by the collective reorganization of orientational correlations, and highlight the value of combining calorimetry, diffraction, neutron spectroscopy, and simulation to resolve disorder-disorder transitions in molecular crystals.

ACKNOWLEDGMENTS

We acknowledge support from the Spanish Ministry of Science, Innovation and Universities under Grant No. MCIN/AEI/10.13039/501100011033, from the European Union European Regional Development Fund (FEDER) under Project No. PID2023-146623NB-I00, and under the "María de Maeztu" Program for Units of Excellence (Grant No. CEX2023-001300-M), as well as from the Generalitat de Catalunya (Grant No. 2021SGR-00343). D. Aguilà acknowledges support from the Spanish Ministry of Science and Innovation through Project No. CNS2022-135816. J.-Ll. Tamarit is grateful to the ICREA Academia program. M.R. is a Serra Húnter fellow. We thank the ISIS Neutron and Muon Source for the provision of beamtime on the OSIRIS spectrometer (RB1720316 [56]), as well as the Institut Laue–Langevin (ILL) for beamtime on the IN16B spectrometer (Experiment 6-05-1084 [57]).

DATA AVAILABILITY

Some of the data that support the findings of this article are openly available [34,56,57]; embargo periods may apply. DSC thermogram and MD simulations data are not publicly available upon publication because it is not technically feasible and/or the cost of preparing, depositing, and hosting the data would be prohibitive within the terms of this research project. The data are available from the authors upon reasonable request.

[1] J. N. Sherwood, *The Plastically Crystalline State: Orientationally-Disordered Crystals* (Wiley, New York, NY, 1979).
[2] P. G. Debenedetti and F. H. Stillinger, Nature (London) **410**, 259 (2001).
[3] A. Meresse, N.-B. Chanh, J.-R. Housty, and Y. Haget, J. Phys. Chem. Solids **47**, 1019 (1986).
[4] N. Chanh, Y. Haget, A. Meresse, and J. Housty, Mol. Cryst. Liq. Cryst. **45**, 307 (1978).
[5] N. Chanh, J. Clastre, J. Gaultier, Y. Haget, A. Meresse, J. Lajzerowicz, A. Filhol, and M. Thomas, J. Appl. Crystallogr. **21**, 10 (1988).
[6] C. Domb, *Phase Transitions and Critical Phenomena*, Vol. 19 (Elsevier, Amsterdam, 2000).
[7] I. S. Aranson and L. Kramer, Rev. Mod. Phys. **74**, 99 (2002).
[8] E. L. Gromnitskaya, I. V. Danilov, and V. V. Brazhkin, Phys. Chem. Chem. Phys. **23**, 2349 (2021).
[9] A. Planes and A. Saxena, *Phase Transitions: A Materials Perspective* (Cambridge University Press, Cambridge, UK, 2025).
[10] B. Parat, L. C. Pardo, M. Barrio, J. Ll. Tamarit, P. Negrier, J. Salud, D. O. López, and D. Mondieig, Chem. Mater. **17**, 3359 (2005).
[11] M. Barrio, J. Ll. Tamarit, P. Negrier, L. C. Pardo, N. Veglio, and D. Mondieig, New J. Chem. **32**, 232 (2008).
[12] M. Zuriaga, M. Carignano, and P. Serra, J. Chem. Phys. **135**, 044504 (2011).
[13] M. Zuriaga, S. Perez, L. C. Pardo, and J. Ll. Tamarit, J. Chem. Phys. **137**, 054506 (2012).
[14] N. B. Caballero, M. Zuriaga, M. Carignano, and P. Serra, J. Phys. Chem. B **120**, 860 (2016).
[15] M. Moratalla, J. F. Gebbia, M. A. Ramos, L. C. Pardo, S. Mukhopadhyay, S. Rudić, F. Fernandez-Alonso, F. J. Bermejo, and J. Ll. Tamarit, Phys. Rev. B **99**, 024301 (2019).

[16] M. Romanini, P. Negrier, J. Ll. Tamarit, S. Capaccioli, M. Barrio, L. C. Pardo, and D. Mondieig, Phys. Rev. B **85**, 134201 (2012).
[17] P. Negrier, M. Barrio, M. Romanini, J. Ll. Tamarit, D. Mondieig, A. I. Krivchikov, L. Kepinski, A. Jezowski, and D. Szewczyk, Crystal Growth Design **14**, 2626 (2014).
[18] D. Szewczyk, A. Jezowski, G. Vdovichenko, A. Krivchikov, F. J. Bermejo, J. Ll. Tamarit, L. C. Pardo, and J. W. Taylor, J. Phys. Chem. B **119**, 8468 (2015).
[19] M. Romanini, J. Ll. Tamarit, L. C. Pardo, F. J. Bermejo, R. Fernandez-Perea, and F. L. Pratt, J. Phys.: Condens. Matter **29**, 085405 (2017).
[20] B. Cui, J. F. Gebbia, M. Romanini, S. Rudić, R. Fernandez-Perea, F. J. Bermejo, J.-Ll. Tamarit, and A. Zaccone, Phys. Rev. B **101**, 104202 (2020).
[21] B. B. Hassine, P. Negrier, M. Romanini, M. Barrio, R. Macovez, A. Kallel, D. Mondieig, and J. Ll. Tamarit, Phys. Chem. Chem. Phys. **18**, 10924 (2016).
[22] L. Yuan, S. Clevers, A. Burel, P. Negrier, M. d. Barrio, B. Ben Hassine, D. Mondieig, V. Dupray, J. Ll. Tamarit, and G. Coquerel, Crystal Growth Design **17**, 3395 (2017).
[23] D. Szewczyk, J. F. Gebbia, A. Jeżowski, A. I. Krivchikov, T. Guidi, C. Cazorla, and J.-Ll. Tamarit, Sci. Rep. **11**, 18640 (2021).
[24] M. Romanini, M. Barrio, S. Capaccioli, R. Macovez, M. D. Ruiz-Martin, and J. Ll. Tamarit, J. Phys. Chem. C **120**, 10614 (2016).
[25] J. F. Gebbia, M. A. Ramos, D. Szewczyk, A. Jezowski, A. I. Krivchikov, Y. V. Horbatenko, T. Guidi, F. J. Bermejo, and J. Ll. Tamarit, Phys. Rev. Lett. **119**, 215506 (2017).
[26] J. F. Gebbia, A. H. Aristizabal, P. Negrier, D. Aguilà, J. Ll. Tamarit, and L. C. Pardo, Phys. Chem. Chem. Phys. **25**, 30553 (2023).
[27] D. Szewczyk, M. Moratalla, G. Chajewski, J. F. Gebbia, A. Jeżowski, A. I. Krivchikov, M. Barrio, J. Ll. Tamarit, and M. A. Ramos, Phys. Rev. B **110**, 174204 (2024).
[28] C. P. Brock and Y. Fu, Acta Crystallogr. Sect. B **53**, 613 (1997).
[29] G. M. Sheldrick, *SAINT and SADABS* (Bruker AXS Inc., Madison, WI, 2012).
[30] G. M. Sheldrick, Acta Crystallogr. Sect. A **71**, 3 (2015).
[31] G. M. Sheldrick, Acta Crystallogr. Sect. C **71**, 3 (2015).
[32] O. Dolomanov, L. Bourhis, R. Gildea, J. Howard, and H. Puschmann, J. Appl. Crystallogr. **42**, 339 (2009).
[33] See Supplemental Material at http://link.aps.org/supplemental/10.1103/pcsf-sfml for additional crystallographic information, including Table S1 (single-crystal data and refinement for phase II), Table S2 (Rietveld refinements of phases II and I), Table S3 (temperature dependence of lattice parameters), Table S4 (fractional atomic coordinates of phase II) Table S5 (anisotropic displacement parameters of phase II), Table S6 (fractional atomic coordinates of phase I), and Fig. S1 (unit cell volume as a function of temperature), and for additional information on the model selection used in the QENS analysis, including Fig. S2 (Probability Distribution Function of the χ^2 for model tested using FABADA).
[34] Crystallographic data for the structures reported in this paper have been deposited at the Cambridge Crystallographic Data Centre (CCDC) and can be obtained free of charge at https://summary.ccdc.cam.ac.uk/structure-summary-form.
[35] M. T. F. Telling and K. H. Andersen, Phys. Chem. Chem. Phys. **7**, 1255 (2005).
[36] M. T. F. Telling, S. I. Campbell, D. Engberg, D. M. Marero, and K. H. Andersen, Phys. Chem. Chem. Phys. **18**, 8243 (2016).
[37] F. Demmel, D. McPhail, C. French, D. Maxwell, S. Harrison, J. Boxall, N. Rhodes, S. Mukhopadhyay, I. Silverwood, V. G. Sakai, *et al.*, J. Phys.: Conf. Ser. **1021**, 012027 (2018).
[38] F. Demmel, A. Perrichon, D. McPhail, P. L. Dapica, N. Webb, A. Cook, E. Schooneveld, J. Boxall, N. Rhodes, C. Lockett, *et al.*, EPJ Web Conf. **286**, 03005 (2023).
[39] O. Arnold, J. Bilheux, J. Borreguero, A. Buts, S. Campbell, L. Chapon, M. Doucet, N. Draper, R. F. Leal, M. Gigg, V. Lynch, A. Markvardsen, D. Mikkelson, R. Mikkelson, R. Miller, K. Palmen, P. Parker, G. Passos, T. Perring, and P. Peterson, *et al.*, Nucl. Instrum. Methods Phys. Res. Sect. A **764**, 156 (2014).
[40] L. C. Pardo, M. Rovira-Esteva, S. Busch, J. F. Moulin, and J. Ll. Tamarit, Phys. Rev. E **84**, 046711 (2011).
[41] D. Monserrat, A. Vispa, L. C. Pardo, R. Tolchenov, S. Mukhopadhyay, and F. Fernandez-Alonso, J. Phys.: Conf. Ser. **663**, 012009 (2015).
[42] B. Frick, J. Combet, and L. van Eijck, Nucl. Instrum. Methods Phys. Res. Sect. A **669**, 7 (2012).
[43] S. Mukhopadhyay, B. Hewer, S. Howells, and A. Markvardsen, Physica B **563**, 41 (2019).
[44] B. R. Brooks, C. L. Brooks III, A. D. Mackerell, L. Nilsson, R. J. Petrella, B. Roux, Y. Won, G. Archontis, C. Bartels, S. Boresch, A. Caflisch, L. Caves, Q. Cui, A. R. Dinner, M. Feig, S. Fischer, J. Gao, M. Hodoscek, W. Im, and K. Kuczera, *et al.*, J. Comput. Chem. **30**, 1545 (2009).
[45] V. Zoete, M. A. Cuendet, A. Grosdidier, and O. Michielin, J. Comput. Chem. **32**, 2359 (2011).
[46] M. Bugnon, M. Goullieux, U. F. Rohrig, V. Zoete, and O. Michielin, J. Chem. Inf. Model. **63**, 6469 (2023).
[47] L. C. Pardo, Angula: Analysis tool developed by Luis Carlos Pardo (UPC), https://gcm.upc.edu/en/members/luis-carlos/angula/ANGULA.
[48] T. L. Khotsyanova, T. A. Babushkina, S. I. Kuznetsov, and G. K. Semin, Kristallografiya **17**, 552 (1972).
[49] A. H. White, B. Biggs, and S. Morgan, J. Am. Chem. Soc. **62**, 16 (1940).
[50] A. Moreno, A. Alegrıa, J. Colmenero, M. Prager, H. Grimm, and B. Frick, J. Chem. Phys. **115**, 8958 (2001).
[51] A. J. Moreno, A. Alegria, J. Colmenero, and B. Frick, Phys. Rev. B **65**, 134202 (2002).
[52] A. Henao, J. M. Salazar-Rios, E. Guardia, and L. C. Pardo, J. Chem. Phys. **154**, 104501 (2021).
[53] D. Martí, R. Pétuya, E. Bosoni, A.-C. Dublanchet, S. Mohr, and F. Léonforte, ACS Appl. Polym. Mater. **6**, 4449 (2024).
[54] H. Gudla and L. Zhang, J. Phys. Chem. B **128**, 10537 (2024).
[55] M. A. F. Afzal, A. R. Browning, A. Goldberg, M. D. Halls, J. L. Gavartin, T. Morisato, T. F. Hughes, D. J. Giesen, and J. E. Goose, ACS Appl. Polym. Mater. **3**, 620 (2020).

[56] J. Ll. Tamarit, S. Mukhopadhyay, L. C. Pardo-Soto, J. Bermejo, and J. F. Gebbia, Glassy dynamics in a model-system: The monoclinic phase of tetrachloromethylxylene, TCMX (C6Cl4(CH3)2), STFC ISIS Facility (2018), doi:10.5286/ISIS.E.94114846.

[57] J. F. Gebbia, M. Appel, L. C. Pardo, and J. Ll. Tamarit, On the microscopic dynamics of the monoclinic phase of tetrachlorometaxylene, TCMX (C6Cl4(CH3)2), Institut Laue-Langevin (ILL) (2024), doi:10.5291/ILL-DATA.6-05-1084.